

Magnetodynamics of few-nanoparticle chains

Thinh Q. Bui^{1,*}, Samuel D. Oberdick^{3,4}, Frank M. Abel², Michael J. Donahue⁵, Klaus N. Quelhas¹, Cindi L. Dennis², Thomas Cleveland^{2,6}, Yanxin Liu^{6,7}, and Solomon I. Woods¹

¹Physical Measurement Laboratory, National Institute of Standards and Technology, Gaithersburg, MD, USA 20899

²Materials Measurement Laboratory, National Institute of Standards and Technology, Gaithersburg, MD, USA 20899

³Physical Measurement Laboratory, National Institute of Standards and Technology, Boulder, CO, USA 80305

⁴Department of Physics, University of Colorado, Boulder, CO, USA 20899

⁵Information Technology Laboratory, National Institute of Standards and Technology, Gaithersburg, MD, USA 20899

⁶Institute for Bioscience and Biotechnology Research (IBBR), Rockville, MD, USA 20850

⁷Department of Chemistry and Biochemistry, University of Maryland, College Park, MD, USA 20742

*e-mail: thinh.bui@nist.gov

ABSTRACT

In recent years, there has been increasing interest in the understanding and application of nanoparticle assemblies driven by external fields. Although these systems can exhibit marked transitions in behavior compared to non-interacting counterparts, it has often proven challenging to connect their dynamics with underlying physical mechanisms or even to verifiably establish their structure under realistic experimental conditions. We have studied colloidal iron oxide nanoparticles that assemble into ordered, few-particle linear chains under the influence of oscillating and pulsed magnetic fields. Cryo-EM has been used to flash freeze and image the structures formed by oscillatory drive fields, and magnetic relaxometry has been used to extract the multiple time constants associated with magnetic switching of the short chains. Armed with the physical structure from cryo-EM and the field-dependent switching times from magnetic measurements, we have conducted extensive micromagnetic simulations, revealing probable mechanisms for each time constant regime spanning 10^9 in time and how switching develops from individual particles to entire chains. These types of magnetic nanomaterials have great potential for biomedical technologies, particularly magnetic particle imaging and hyperthermia, and rigorous elucidation of their physics will hasten their optimization.

Key points: magnetic nanoparticles, nanoscale assembly, superferromagnetism, magnetic particle imaging, magnetization dynamics, magnetometry

Introduction

Magnetic nanoparticles (MNPs) less than 25 nm diameter are often composed of a single magnetic domain and each nanoparticle can behave like a superspin building block in systems of MNPs. Interacting MNPs exhibit a rich variety of behavior including super spin-glass, superparamagnetism with relaxation, and superferromagnetism¹⁻⁴. When magnetically-interacting MNPs are dispersed in liquid solvent rather than solid matrix, the complexity of particle dynamics is even greater. In response to magnetic fields, the magnetic moment can switch by internal spin dynamics (Néel mode) and by physical rotation (Brownian mode)⁵⁻⁷. Furthermore, particles can assemble under fields through translational and rotational motion in the fluid, leading to dynamic change of inter-particle interactions^{8,9}. The prospect of controllable and reversible assembly is indeed intriguing, from the perspective of utilizing MNPs as functional constituents for artificial materials and devices^{10,11}. Dynamics of ferrofluids can be so complex that experimental and computational studies often consider Néel and Brownian mechanisms in isolation, but in a few cases the more realistic situation where both can operate simultaneously has been considered^{5,7,12,13}. Fluid MNP materials that display 1-D chaining of particles have been harnessed to significantly boost the performance of magnetic particle imaging (MPI) tracers and heating by hyperthermia¹⁴⁻¹⁷. These materials have been the focus of intense research in recent years, but the physical mechanisms responsible for their distinctive dynamics are still unclear.

We have developed ferrofluids composed of field-assisted 1-D chain assemblies of iron-oxide nanoparticles, and show how the simultaneous action of Néel and Brownian mechanisms leads to their distinctive dynamic response to pulsed and oscillating magnetic fields. Distinct from more complex chain assemblies in ferrofluids¹⁸⁻²¹, our system is particularly simple, where the linear chains are relatively short (≈ 4 MNPs) and only dipolar interactions between particles are active because the MNPs are coated by a thin non-magnetic shell. Cryo-EM imaging has been used to capture the geometry of these structures when driven by magnetic fields that promote inter-particle interactions, providing essential information for micromagnetic simulations.

The magnetodynamics of these short chains are probed with custom magnetic instrumentation to isolate the separate Néel and Brownian steps involved in switching of the chains over timescales from 1 μ s to 10 s. These instruments are members

of a class of novel magnetic spectrometers and relaxometers that have been developed over the last decade^{17,22,23} to probe MNPs at amplitudes high enough to drive the non-linear response required for MPI and probe the timescales relevant for Néel and Brownian relaxation near room temperature. The strategy in this work is to quantify the dynamics by determining time constants and switching amplitudes from the relaxometry data and comparing with estimated time constants and results of Landau–Lifshitz–Gilbert (LLG) simulations^{24,25}. In contrast to isolated nanoparticles, our linear chains exhibit strongly-hysteretic magnetization curves and a 3-step relaxation process. Direct comparison of the magnetic data with simulations enables us to discriminate between Néel and Brownian processes and connect each step in the relaxation process with different physical mechanisms (e.g., single-particle Néel, chain Néel, Brownian rotation of chains).

Magnetometry of SPM and SFM nanoparticles

Stable colloidal dispersions of small, single-domain magnetic nanoparticles driven by external magnetic fields typically exhibit superparamagnetic (SPM) behavior at room temperature with zero net magnetization at zero field^{26,27}. These SPM nanoparticles align with the applied external field, and if they display sufficiently strong magnetic dipole moment (m) can assemble into larger macro-structures. The propensity for inter-particle interactions is driven by magnetic dipole-dipole interaction energy (scales as m^2/d^3 , where d is the distance between MNP centers), which directly competes with thermal energy that can break the ordering²⁸. Given that m scales with particle volume (V), the interaction energy density E_{int}/V scales with r/d , where r is the MNP radius. At low enough temperatures, the macro-structures can exhibit superferromagnetic (SFM) behavior with hysteretic response and remanent magnetization at zero field. If the field-driven ordered macro-structures dissipate over some timescale due to thermal energy agitation when the external field is removed, the resultant is a transient superferromagnetic (SFM) state that exists at the intersection of SPM and SFM^{3,14,17} in which assembly (ordering) is reversible. Fig. S1 summarizes our SFM systems discussed in this work.

AC magnetometry can readily differentiate between the SPM and SFM states. For an inductive coil measurement of the magnetization response of SPM nanoparticles, the magnetization is ideally described by the field-dependent Langevin function, $L(H)$. Under a sinusoidal excitation field $H(t)$, the voltage induced, $V_i(t)$, in the inductive coil sensor from the particle response is given by:

$$V_i(t) \propto \rho \dot{L}[H(t)] \quad (1)$$

Here, ρ is the density and $\dot{L}[H(t)]$ is the time derivative of the Langevin function. On the other hand, the voltage response of the ideal SFM state is closer to the derivative of a step function, with a phase offset because the step is centered at a non-zero (coercive) field. Figure S2 compares the measured $V_i(t)$ for the SFM and SPM systems. While SPM particles follow approximate Langevin behavior, the response from the SFM is much more sharply peaked with a distinctive phase offset^{29–31}. The significantly broader harmonic spectrum of SFM relative to SPM provides a corresponding sensitivity and spatial resolution boost for MPI¹⁴; see Fig. S3 and caption for details.

One can distinguish between SPM and SFM nanoparticle systems by tuning the applied magnetic field, with SFM macro-structures exhibiting threshold behavior as function of field amplitude as well as strongly hysteretic magnetization (M vs. H) curves. Figure 1 shows this field amplitude dependence of $V_i(t)$, revealing a clear threshold field marking the onset of a sharp rise in the magnetization response. An abrupt transition in the hysteresis loops presented in subpanels ii and iii provides a more intuitive picture of chaining, indicated by a sudden increase in hysteresis near the threshold field of ≈ 8 mT. From remanence measurement (Fig. S4), chained structures decay on timescales from 1 ms to 1 s at zero field, consistent with previous reports^{17,32}. We observed a general trend that all synthesized particles of high crystal quality (magnetite, minimal defects) and whose size exceed a critical diameter of ≈ 15 nm³¹ display SFM-like behavior. The canted square-like hysteresis loop can be explained by a mixed population of single and chained particles (Fig. S5). The smaller synthesized 7 and 10 nm iron oxide nanoparticles (and a commercial MNP sample, Vivotrax) display no threshold and non(weakly)-hysteretic magnetization characteristics, as expected for SPM systems. Finally, below the threshold field, all systems display SPM-like response, regardless of size, strongly implicating the role of a critical threshold field to drive inter-particle interactions into chaining.

Structure and magnetism of iron oxide nanoparticle chains

To unambiguously reveal the physical structure that gives rise to the observed SFM-like magnetization response in our samples, we developed a cryo-TEM method to flash-freeze MNPs under AC fields (Fig. S6). Unlike traditional TEM where drying artifacts may be present, flash-freezing preserves the sample in its native colloidal state. Figure 2 presents microscopy images at field on and off conditions. Different from previous studies that used static (DC) fields with amplitudes > 100 mT, our smaller field amplitude (15 mT, 250 Hz) for short duration (< 5 sec) show only the formation of isolated 1D chains with relatively short lengths, ranging from 3 to 12 nanoparticles, when compared to no field conditions. These measurements conclusively reveal the existence of few particle 1D chains proposed previously^{14,30}. We do not observe more complex 2D or 3D assemblies described

in previous studies^{18,20}, which likely formed from using a larger magnetic field and/or longer field-on time, highlighting the advantage of our cryo-EM procedure to capture these transient intermediate states. Figure 2(c) shows the compiled histogram for the observed chain length distribution at two different concentrations. At double the concentration, the distribution is shifted to longer chain lengths with the mode at 4 nanoparticles per chain.

The manifestation of SFM-like behavior is a balancing act between interparticle interaction energy, E_{int} , which promotes chaining, and thermal energy, $k_B T$, which counteracts it as a dissipative force^{18,20,21}. To understand the energetics and thus the propensity for chain formation, we provide estimates for the interaction energy using the structural information obtained from cryo-TEM. The interaction energy $E_{int}(\vec{d}_{ij})$ of two magnetic dipoles with dipole moments vectors, \vec{m}_i and \vec{m}_j , separated by vector \vec{d} is described by

$$E_{int}(\vec{d}_{ij}) = \frac{\mu_0}{4\pi d_{ij}^3} \left[\vec{m}_i \cdot \vec{m}_j - 3 \frac{(\vec{m}_i \cdot \vec{d}_{ij})(\vec{m}_j \cdot \vec{d}_{ij})}{d_{ij}^2} \right] \quad (2)$$

where μ_0 is the magnetic permeability, $\vec{d}_{ij} = \vec{d}_i - \vec{d}_j$, and $d_{ij} = |\vec{d}_{ij}|$. The nanoparticle magnetic dipole moment was estimated from the saturation magnetization of $M_s = 80 \text{ A} \cdot \text{m}^2/\text{kg}$, to be $m \approx 8 \times 10^4 \mu_B$ for $15 \pm 1 \text{ nm}$ diameter SFM nanoparticles where μ_B is the Bohr magneton. Assuming identical nanoparticles and using a measured edge-to-edge separation of $2.0 \pm 1.7 \text{ nm}$ from cryo-TEM, the calculated magnetic dipole-dipole interaction energy from Eq. 2 equates to $E_{int} = 5 \pm 3 k_B T$. An interaction energy value within the order of thermal energy at room temperature suggests that chaining can be stabilized. The chaining can be sensitive to a modest magnetic field ($< 10 \text{ mT}$) as well because the Zeeman energy ($\approx 2 k_B T$) is also on the order of the thermal energy. Since the energy density for the dipole interaction, anisotropy and Zeeman term are all invariant when particle radius (r) and particle separation (d) are scaled up in tandem (e.g., diameter and separation doubled), the energetics for chaining are the same for any system with the same ratio r/d .

Dynamics of chaining

Under AC magnetic fields, colloidal chaining is dynamic and governed by both Brownian and Néel mechanisms. Initial insights on the dynamics of SFM ordering can be gleaned from the field dependence of the threshold behavior. Since the alignment of the internal magnetic moment and chaining are governed by different dynamic relaxation mechanisms^{6,33}, the SPM-SFM transition threshold is expected to be sensitive to the oscillating field frequency. Figure S7(a) shows an increase in threshold field with increasing drive frequency, likely the result of the relatively slow time constants associated with chain formation/rotation and that higher amplitude fields can drive these processes faster. The gradual decrease in the remanence and coercivity with decreasing frequency in S7(b) is consistent with remanence decay of the transient SFM state and the relatively slow time constants associated with Brownian rotation of chains¹⁴.

Previously, Conolly and coworkers introduced a phenomenological model using a "Langevin saturator" that mimics an electronic Schmitt trigger to describe the square hysteresis loop for chain formation^{14,29,30}. This mean field model captures the important idea that particles in a chain are strongly influenced by the combined dipole fields from neighboring particles, but it does not provide information on the coordinated process of switching along a chain. To elucidate the time dependence of magnetic switching of chains and the underlying physical mechanisms, we performed high speed magnetic relaxometry (MRX)²³ measurements with support from micromagnetics simulations to provide direct insight on the step-by-step dynamics over an extremely broad timescale of nanoseconds to seconds. Here, a fast-rise square pulse magnetic field at different amplitudes below and above the threshold field drives the MNP systems and the steady-state magnetization is measured. Figure 3 shows a comparison of the field amplitude-dependence of the magnetization response for the SPM and SFM systems.

Relative to the SPM system, which has dynamics dominated by a single Brownian process²³, the SFM system at and above the threshold field is significantly more complex, exhibiting multi-step dynamics over the five orders of magnitude in time measured. Below the threshold field ($\approx 6 \text{ mT}$), the SFM particle response is characterized by a single time constant typical for a non-interacting SPM particle. Above the threshold field, the dynamics are governed by a three-step process: the fastest dynamics occurs on the order of nanoseconds, followed by a secondary rise from 100s of nanoseconds to microseconds, then a slow tertiary rise from milliseconds to seconds. An empirical, three-step sigmoidal-Boltzmann growth function was used to extract amplitudes (Fig. 3(c)) and time constants (Fig. 3(d)) from the MRX data:

$$M(t) = a_1 \left(1 - \frac{1}{1 - \exp((t - t_0_1)/\tau_1)} \right) + a_2 \left(1 - \frac{1}{1 - \exp((t - t_0_2)/\tau_2)} \right) * \frac{1 + \frac{\sqrt{(t - t_0_2)^2}}{t - t_0_2}}{2} \quad (3)$$

$$+ a_3 \left(1 - \frac{1}{1 - \exp((t - t_0_3)/\tau_2)} \right) * \frac{1 + \frac{\sqrt{(t - t_0_3)^2}}{t - t_0_3}}{2}.$$

The $\frac{1 + \sqrt{(t-t_0)^2}}{2(t-t_0)}$ components in Eq. 3 act to turn on the second and third step functions when $t > t_0$ to account for a sequential, delayed magnetization response.

Based on a simple estimate of Néel and Brownian response for isolated 15 to 20 nm particles, the first time constant is consistent with Néel rotation of a single nanoparticle faster than 1 μ s. Following the single particle Néel rotation, chain formation and a rapid a spin-reversal avalanche effect facilitated by dipolar interactions initiate in the second step to align the moments of neighboring particles in the chain between 1 to 300 microseconds (step #2 in 3(c) and 3(d)). This avalanche action can be significantly slower than the single particle spin rotation because thermal activation causes random spin depolarization that competes directly with field alignment until sufficient time has elapsed for all particles in a chain to align in concert. Evidence for the onset of chain formation and reversal avalanche is most conspicuous in the fitted amplitude (Fig. 3(c)), which shows the canonical threshold behavior (between 5 to 6 mT) that gives rise to the sharp increase in the magnetization³⁰.

To understand this critical avalanche action in more detail, we performed micromagnetic simulations (OOMMF²⁵) of thermally-activated reversals of chains consisting of four nanoparticle presented in Fig. 4. In these trials the chain is aligned with the arbitrarily defined x-axis, and the magnetization is initialized in the +x direction. At time $t = 0$ ns a (pseudo-random) thermal field representing a temperature of $T = 290$ K is activated²⁴ and a reversing field is applied. If the reversing field is strong enough, then after some time the thermal field can promote the magnetization over the energy barrier associated with the shape anisotropy of the chain. The time to reverse will be random, depending on the thermal field, and Fig. 4(a) shows twelve reversals at 18 mT.

A cumulative distribution function (CDF, see SI for more details) for estimating reversal time constants can be created by accumulating the switching events by time. The CDFs for several different applied fields are presented in Fig. 4(b), and the fitted constants in Fig. S9(c). The time constants predicted by the CDFs correlate well with the step #2 experimental data in Fig. 3(d). Figure 4(c) and 4(d) provide representative details on the switching process for one trial under a 14 mT reversing field. The thick purple curve shows the overall x-axis magnetization, while the thinner curves represent the m_x and m_y components. In Fig. 4(c), the thermal field initiates the reversal by nearly reversing the magnetization of the end particle (particle 4), but its m_x reverses back while the two particles at the opposite end (particles 1 and 2) begin their complete reversal. This is followed by particle 3 and finally particle 4 to complete the chain reversal. Thus, after the initial kick by particle 4, the chain reverses in a cascading fashion from the opposite end. Figure 4(d) shows that this reversal is not a direct cascade, but involves precessional rotation about the chain axis as shown in the m_y data. Moreover, in this rotation neighboring particles are nearly 180° out of phase, with particle 1 and 3, and likewise particle 2 and 4, in near alignment. This is caused by dipolar interactions between neighboring particles.

Finally, to probe the origin of the slow, third time constant (milliseconds to seconds) in the MRX data, an experiment was performed where a sinusoidal magnetic field was turned on at time zero and the magnetization response was continuously recorded and binned in 25 ms intervals (total time of 2 s). This type of measurement tracks the temporal evolution of the hysteresis loops, which will be motivated in the following. Figure 5(a) shows that the SFM magnetization increases over time and does not peak within one cycle of the AC excitation field, as was also observed by Colson *et al.*³⁰; rather, the changing magnetization exhibits a corresponding evolution of the hysteresis curve (increasing coercivity and remanence over time), plotted in Fig. 5(b). Using data from Fig. 5(a), Fig. 5(c) shows the calculated RMS magnetization over time, and reveals that the evolution timescale depends on drive field amplitude. Here, the first point (amplitude) for each measurement trace is not zero, suggesting that fast dynamics prior to 25 ms (single particle Néel moment reversal and chain formation) has occurred. Fits to capture the fast time constant for data in 5(c) are presented in Fig. 5(d), which once again show the threshold behavior for both SFM systems to indicate that chains are responsible for the dynamics. Most interestingly, the gradual growth in the remanence and coercivity over time in Fig. 5(b) is suggestive of a Brownian alignment of the chain axis to an external field, rather than chain growth: the latter mechanism would result in an abrupt increase in the remanence and coercivity between the transition from monomer to dimer and saturate rapidly with increasing chain length (Fig. S10).

Micromagnetic modeling can capture the dynamics and energetics of these rotating chains. To model the data in Fig. 5(b), the hysteresis loops for individual 4-particle chains at various angles to an applied field are computed (see Methods section). Fig. 6(a) shows the cumulative response for a collection of 4-particle chains that are initially randomly oriented in 3D (time $t=0$, arbitrary units). As the chains gradually rotate, the hysteresis loops become increasingly square-like and saturate by $t=10$ when the chains are all nearly aligned with the applied field axis. This result captures all the essential features of the experimental data in Fig. 5(b). Note that thermal effects could explain the observed lower coercivity in the experimental data compared to simulations.

Finally, micromagnetics simulations can shed light on the observed chain length distribution from cryo-TEM data. Fig. 6(b) gives the magnetic energy density in nanoparticle chains of various lengths as a function of an on-axis applied field. At all fields the energy density is less for longer chains, so it is energetically favorable for short chains to lengthen. This energy reduction saturates beyond six nanoparticles, allowing other forces in the system to limit chain length. This is consistent with

mode of the chain length population distribution at a few nanoparticles with very few chains longer than 8 nanoparticles.

In this work, we have experimentally shown the distinct, in-depth magnetization dynamics of superparamagnetic nanoparticles below and above a critical size for chaining. Few-particle chains (< 5 nanoparticles) provide orders of magnitude gain in magnetization response compared to single particles, so the development of nanoscale vehicles that can robustly stabilize these chains in solid matrix will have important future technological implications. Our micromagnetic modeling indicates that the magnetization characteristic and fast chain switching dynamics are captured by Néel mechanisms, which will be preserved in solid systems. From a computational perspective, these relatively simple MNP assemblies could aid to advance all-atom simulations to account for complex contributions from the solvent and ligand composition of the shell on magnetodynamics³⁴, critical for applications that use nanoparticles including soft robotics, directed drug delivery, and biological sensing. Finally, the presented dynamics of interacting MNPs could be fundamental for the understanding of phase transitions in dipolar fluids³⁵ bli

References

1. Jonsson, T., Nordblad, P. & Svedlindh, P. Dynamic study of dipole-dipole interaction effects in a magnetic nanoparticle system. *Phys. Rev. B* **57**, 497–504, DOI: [10.1103/PhysRevB.57.497](https://doi.org/10.1103/PhysRevB.57.497) (1998).
2. Jonsson, T., Svedlindh, P. & Hansen, M. F. Static scaling on an interacting magnetic nanoparticle system. *Phys. Rev. Lett.* **81**, 3976–3979, DOI: [10.1103/PhysRevLett.81.3976](https://doi.org/10.1103/PhysRevLett.81.3976) (1998).
3. Mørup, S., Hansen, M. F. & Frandsen, C. Magnetic interactions between nanoparticles. *Beilstein J Nanotechnol* **1**, 182–190 (2010).
4. Zeleňáková, A. *et al.* Superferromagnetism in chain-like Fe@SiO₂ nanoparticle ensembles. *J. Appl. Phys.* **116**, 033907, DOI: [10.1063/1.4890354](https://doi.org/10.1063/1.4890354) (2014).
5. Berkov, D. Micromagnetic simulations of the magnetization dynamics in nanostructures with special applications to spin injection. *J. Magn. Magn. Mater.* **300**, 159–163, DOI: <https://doi.org/10.1016/j.jmmm.2005.10.055> (2006).
6. Deissler, R. J., Wu, Y. & Martens, M. A. Dependence of brownian and néel relaxation times on magnetic field strength. *Med. Phys.* **41**, 012301, DOI: <https://doi.org/10.1118/1.4837216> (2014).
7. Ota, S. & Takemura, Y. Characterization of néel and brownian relaxations isolated from complex dynamics influenced by dipole interactions in magnetic nanoparticles. *The J. Phys. Chem. C* **123**, 28859–28866, DOI: [10.1021/acs.jpcc.9b06790](https://doi.org/10.1021/acs.jpcc.9b06790) (2019).
8. Faraudo, J., Andreu, J. S., Calero, C. & Camacho, J. Predicting the self-assembly of superparamagnetic colloids under magnetic fields. *Adv. Funct. Mater.* **26**, 3837–3858, DOI: <https://doi.org/10.1002/adfm.201504839>.
9. Anderson, N. R., Davidson, J., Louie, D. R., Serantes, D. & Livesey, K. L. Simulating the self-assembly and hysteresis loops of ferromagnetic nanoparticles with sticking of ligands. *Nanomater. (Basel)* **11**, 2870 (2021).
10. Nie, Z., Petukhova, A. & Kumacheva, E. Properties and emerging applications of self-assembled structures made from inorganic nanoparticles. *Nat. Nanotechnol.* **5**, 15–25 (2010).
11. Bao, Y., Wen, T., Samia, A. C. S., Khandhar, A. & Krishnan, K. M. Magnetic nanoparticles: Material engineering and emerging applications in lithography and biomedicine. *J Mater Sci* **51**, 513–553 (2015).
12. Weizenecker, J. The Fokker-Planck equation for coupled Brown-Néel-rotation. *Phys Med Biol* **63**, 035004 (2018).
13. Draack, S. *et al.* Determination of dominating relaxation mechanisms from temperature-dependent magnetic particle spectroscopy measurements. *J. Magn. Magn. Mater.* **474**, 570–573, DOI: <https://doi.org/10.1016/j.jmmm.2018.11.023> (2019).
14. Tay, Z. W. *et al.* Superferromagnetic nanoparticles enable order-of-magnitude resolution & sensitivity gain in magnetic particle imaging. *Small Methods* **5**, 2100796, DOI: [10.1002/smt.202100796](https://doi.org/10.1002/smt.202100796) (2021).
15. Nemati, Z. *et al.* Enhanced magnetic hyperthermia in iron oxide nano-octopods: Size and anisotropy effects. *The J. Phys. Chem. C* **120**, 8370–8379, DOI: [10.1021/acs.jpcc.6b01426](https://doi.org/10.1021/acs.jpcc.6b01426) (2016).
16. Mille, N. *et al.* Probing dynamics of nanoparticle chains formation during magnetic hyperthermia using time-dependent high-frequency hysteresis loops. *Appl. Phys. Lett.* **119**, 022407, DOI: [10.1063/5.0056449](https://doi.org/10.1063/5.0056449) (2021).
17. Fung, K. L. B. *et al.* First superferromagnetic remanence characterization and scan optimization for super-resolution magnetic particle imaging. *Nano Lett.* **23**, 1717–1725, DOI: [10.1021/acs.nanolett.2c04404](https://doi.org/10.1021/acs.nanolett.2c04404) (2023). PMID: 36821385.
18. Butter, K., Bomans, P. H. H., Frederik, P. M., Vroege, G. J. & Philipse, A. P. Direct observation of dipolar chains in iron ferrofluids by cryogenic electron microscopy. *Nat. Mater.* **2**, 88–91, DOI: [10.1038/nmat811](https://doi.org/10.1038/nmat811) (2003).

19. Lalatonne, Y., Richardi, J. & Pileni, M. P. Van der waals versus dipolar forces controlling mesoscopic organizations of magnetic nanocrystals. *Nat. Mater.* **3**, 121–125 (2004).
20. Taheri, S. M. *et al.* Self-assembly of smallest magnetic particles. *Proc. Natl. Acad. Sci.* **112**, 14484–14489, DOI: [10.1073/pnas.1511443112](https://doi.org/10.1073/pnas.1511443112) (2015).
21. Chen, Y. & El-Ghazaly, A. Self-assembly of magnetic nanochains in an intrinsic magnetic dipole force-dominated regime. *Small* **19**, 2205079, DOI: <https://doi.org/10.1002/smll.202205079> (2023).
22. Tay, Z. W. *et al.* A High-Throughput, Arbitrary-Waveform, MPI spectrometer and relaxometer for comprehensive magnetic particle optimization and characterization. *Sci. Reports* **6**, 34180 (2016).
23. Bui, T. Q. *et al.* Advanced characterization of magnetization dynamics in iron oxide magnetic nanoparticle tracers. *Appl. Phys. Lett.* **120**, 012407, DOI: [10.1063/5.0077016](https://doi.org/10.1063/5.0077016) (2022).
24. García-Palacios, J. L. & Lázaro, F. J. Langevin-dynamics study of the dynamical properties of small magnetic particles. *Phys. Rev. B* **58**, 14937–14958, DOI: [10.1103/PhysRevB.58.14937](https://doi.org/10.1103/PhysRevB.58.14937) (1998).
25. Donahue, M. & Porter, D. Oommf user's guide, version 1.0. *NISTIR 6376*, *Natl. Inst. Standards Technol. Gaithersburg, MD, USA.* (1999). <https://math.nist.gov/oommf/>.
26. Kaiser, R. & Miskolczy, G. Magnetic Properties of Stable Dispersions of Subdomain Magnetite Particles. *J. Appl. Phys.* **41**, 1064–1072, DOI: [10.1063/1.1658812](https://doi.org/10.1063/1.1658812) (1970). https://pubs.aip.org/aip/jap/article-pdf/41/3/1064/10562677/1064_1_online.pdf.
27. Hu, M. *et al.* Shaping the assembly of superparamagnetic nanoparticles. *ACS Nano* **13**, 3015–3022, DOI: [10.1021/acsnano.8b07783](https://doi.org/10.1021/acsnano.8b07783) (2019). PMID: 30802035.
28. Andreu, J. S., Camacho, J. & Faraudo, J. Aggregation of superparamagnetic colloids in magnetic fields: The quest for the equilibrium state. *Soft Matter* **7**, 2336–2339, DOI: [10.1039/c0sm01424a](https://doi.org/10.1039/c0sm01424a) (2011).
29. Saayujya, C., Fung, K. L. B. & Colson, C. Computational modeling of superferromagnetism in finite-length chains of superparamagnetic Iron Oxide tracers for use in super-resolution Magnetic Particle Imaging. *Int. J. on Magn. Part. Imaging IJMPI* **8**, 8–11 (2022).
30. Colson, C. *et al.* Evidence that spio chain formation is essential for high-resolution mpi. *bioRxiv* DOI: [10.1101/2022.11.27.518061](https://doi.org/10.1101/2022.11.27.518061) (2022).
31. Abel, F. M. *et al.* Strongly interacting nano-ferrites for magnetic particle imaging and spatially resolved thermometry. *ACS Appl. Mater. & Interfaces* (under revision).
32. Fung, K. L. B., Colson, C. & Fellows, B. D. Elucidating super-resolution Magnetic Particle Imaging : superferromagnetic remanence decay through MPI signal evolution informs super-resolution MPI scan strategies. *Int. J. on Magn. Part. Imaging IJMPI* **8**, 8–11 (2022).
33. Eberbeck, D., Wiekhorst, F., Steinhoff, U. & Trahms, L. Aggregation behaviour of magnetic nanoparticle suspensions investigated by magnetorelaxometry. *J. Physics: Condens. Matter* **18**, S2829, DOI: [10.1088/0953-8984/18/38/S20](https://doi.org/10.1088/0953-8984/18/38/S20) (2006).
34. Mahmood, A. U. & Yingling, Y. G. All-atom simulation method for zeeman alignment and dipolar assembly of magnetic nanoparticles. *J. Chem. Theory Comput.* **18**, 3122–3135, DOI: [10.1021/acs.jctc.1c01253](https://doi.org/10.1021/acs.jctc.1c01253) (2022). PMID: 35271259, <https://doi.org/10.1021/acs.jctc.1c01253>.
35. Tlusty, T. & Safran, S. A. Defect-induced phase separation in dipolar fluids. *Science* **290**, 1328–1331, DOI: [10.1126/science.290.5495.1328](https://doi.org/10.1126/science.290.5495.1328) (2000). <https://www.science.org/doi/pdf/10.1126/science.290.5495.1328>.
36. Sun, S. & Zeng, H. Size-Controlled Synthesis of Magnetite Nanoparticles. *J. Am. Chem. Soc.* **124**, 8204–8205, DOI: [10.1021/ja026501x](https://doi.org/10.1021/ja026501x) (2002).
37. Moya, C., Morales, M. d. P., Batlle, X. & Labarta, A. Tuning the magnetic properties of co-ferrite nanoparticles through the 1,2-hexadecanediol concentration in the reaction mixture. *Phys. Chem. Chem. Phys.* **17**, 13143–13149, DOI: [10.1039/C5CP01052G](https://doi.org/10.1039/C5CP01052G) (2015).
38. Nedelkoski, Z. *et al.* Origin of reduced magnetization and domain formation in small magnetite nanoparticles. *Sci. Reports* **7**, 45997 (2017).
39. Bui, T. Q., Henn, M.-A., Tew, W. L., Catterton, M. A. & Woods, S. I. Harmonic dependence of thermal magnetic particle imaging. *Sci. Reports* **13**, 15762, DOI: [10.1038/s41598-023-42620-1](https://doi.org/10.1038/s41598-023-42620-1) (2023).
40. Nguyen, H. P. M., McGuire, K. L., Cook, B. D. & Herzik, M. A., Jr. Manual Blot-and-Plunge Freezing of Biological Specimens for Single-Particle Cryogenic Electron Microscopy. *J. Vis. Exp.* 62765, DOI: [10.3791/62765](https://doi.org/10.3791/62765) (2022).

41. Mastronarde, D. N. Automated electron microscope tomography using robust prediction of specimen movements. *J. Struct. Biol.* **152**, 36–51, DOI: [10.1016/j.jsb.2005.07.007](https://doi.org/10.1016/j.jsb.2005.07.007) (2005).
42. Zivanov, J. *et al.* New tools for automated high-resolution cryo-em structure determination in relion-3. *eLife* **7**, e42166, DOI: [10.7554/eLife.42166](https://doi.org/10.7554/eLife.42166) (2018).
43. Goodwill, P. W. & Conolly, S. M. The x-space formulation of the magnetic particle imaging process: 1-d signal, resolution, bandwidth, snr, sar, and magnetostimulation. *IEEE Transactions on Med. Imaging* **29**, 1851–1859, DOI: [10.1109/TMI.2010.2052284](https://doi.org/10.1109/TMI.2010.2052284) (2010).
44. Croft, L. R., Goodwill, P. W. & Conolly, S. M. Relaxation in x-space magnetic particle imaging. *IEEE Trans Med Imaging* **31**, 2335–2342 (2012).

Figures and Figure Captions

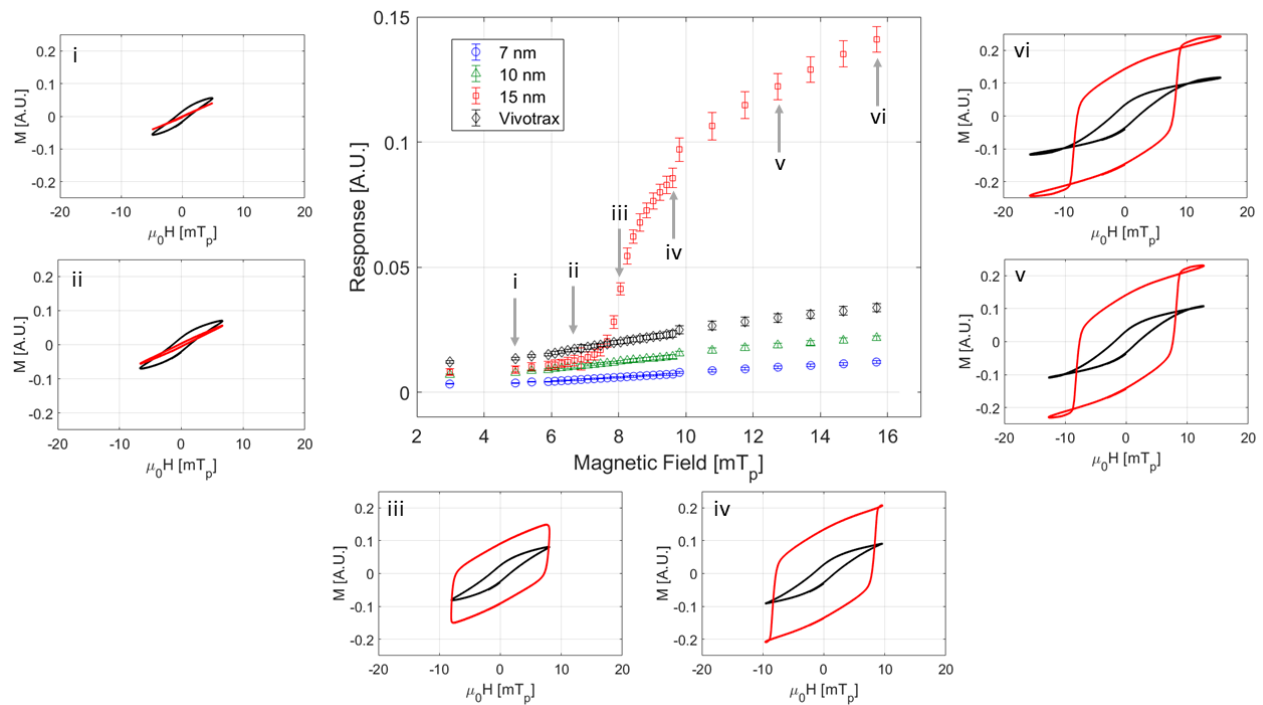


Figure 1. Threshold behavior of chaining nanoparticles. **Middle panel** - Magnetization response for MNPs of four different sizes at different field amplitudes and fixed frequency of 20 kHz. Only one (15 nm, SFM #1) shows the threshold behavior marked as region iii (near threshold field) in the middle panel. Vivotrax is a commercial iron oxide MNP aggregate of single nanoparticles with diameter below 10 nm. **Sub panels** - comparison of the hysteresis loops for the chaining particle (15 nm, red) and a Vivotrax (black) at the six different magnetic field points on the curve in the middle panel (i to vi markers indicated by the gray arrows). For Vivotrax, the hysteresis loops change negligibly compared to the 15 nm particle, which shows an abrupt loop opening in the transition near the threshold field between regions ii and iii.

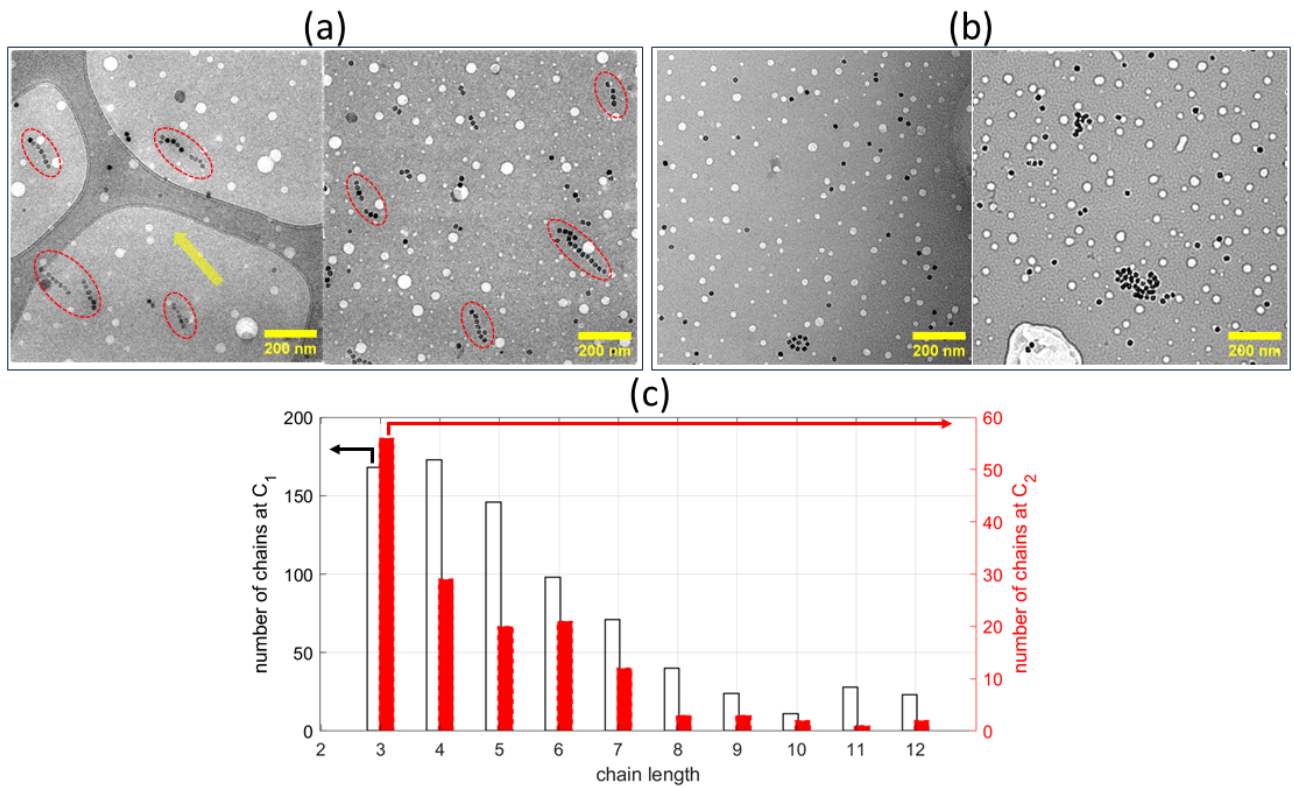


Figure 2. Cryo-EM measurements of SFM assembly in a 250 Hz, 15 mT sinusoidal magnetic field. Panels (a) and (b) show images with the magnetic ON and OFF, respectively. The dashed ovals indicate MNP chains composed of individual nanoparticles (black dots). The yellow arrow in (a) point to the magnetic field direction. Panel (c) is a histogram for the distribution of chain lengths (in units of number of particles) at two SFM concentrations C_1 and C_2 , where $C_1 = 2C_2$. Here, the concentrations are $C_1 \approx 0.34$ mg/ml and $C_2 \approx 0.17$ mg/ml.

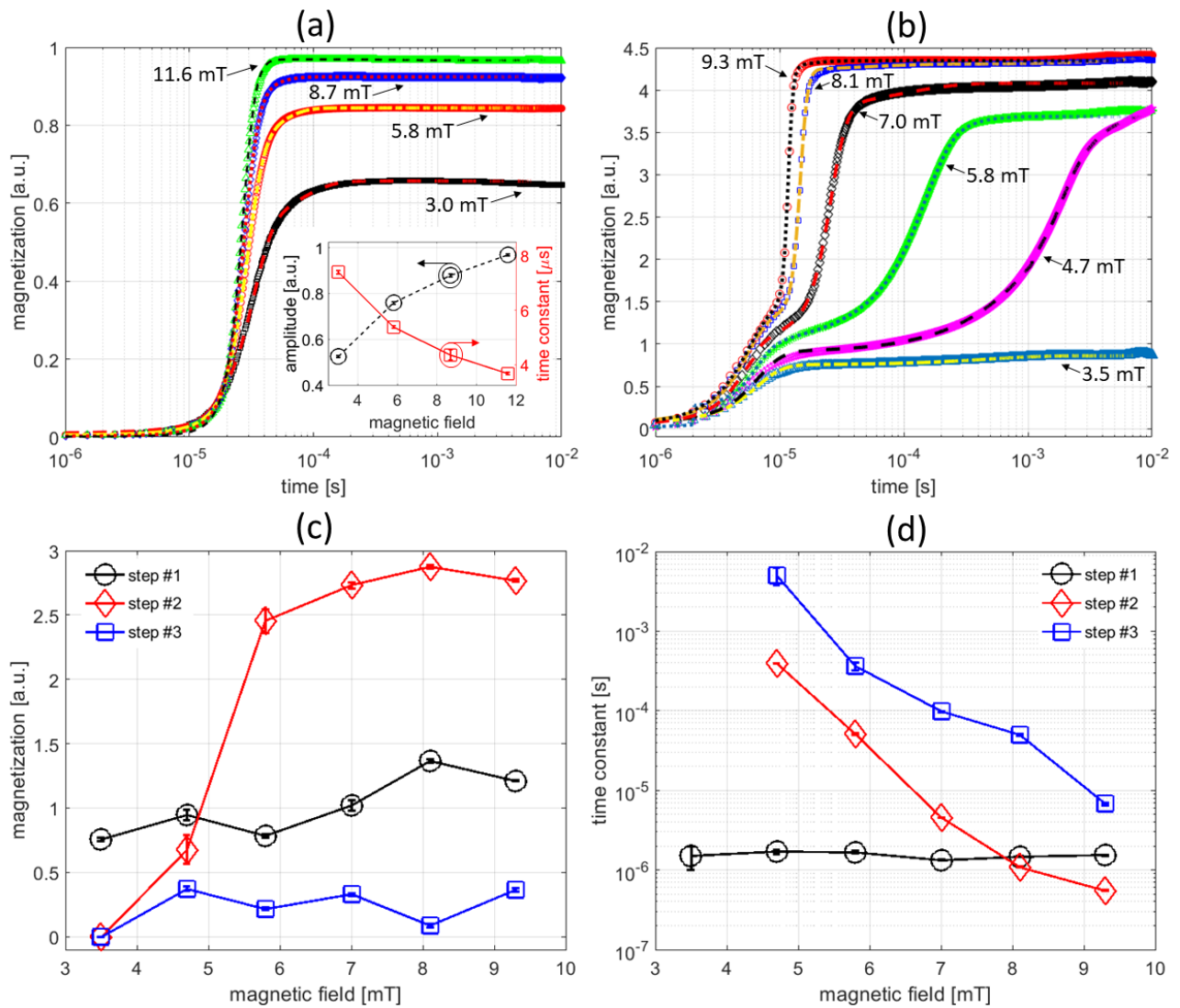


Figure 3. MRX (pulsed) measurement. Field-on magnetization of (a) SPM and (b) SFM systems at different field amplitudes. The data and corresponding fits using Eq. 3 are indicated by data points and lines (solid/dashed), respectively. The inset in (a) shows the fitted amplitude and time constant for SPM system. (c) and (d) show the fitted amplitudes and time constants, respectively, for the SFM particles in (b). The solid lines in (c) and (d) are connecting lines for visual guide and not fits to the data. The "step #" in the legend pertains to the three distinct steps in the MRX data. Step #2 shows the threshold behavior for the magnetization amplitude and displays the largest decrease in the time constants with increasing magnetic field, indicating that it is the chain formation and spin-reversal avalanche step for the entire chain. This property of SFM systems contrasts the nearly linear field-dependence for the SPM system displayed in the inset of (a).

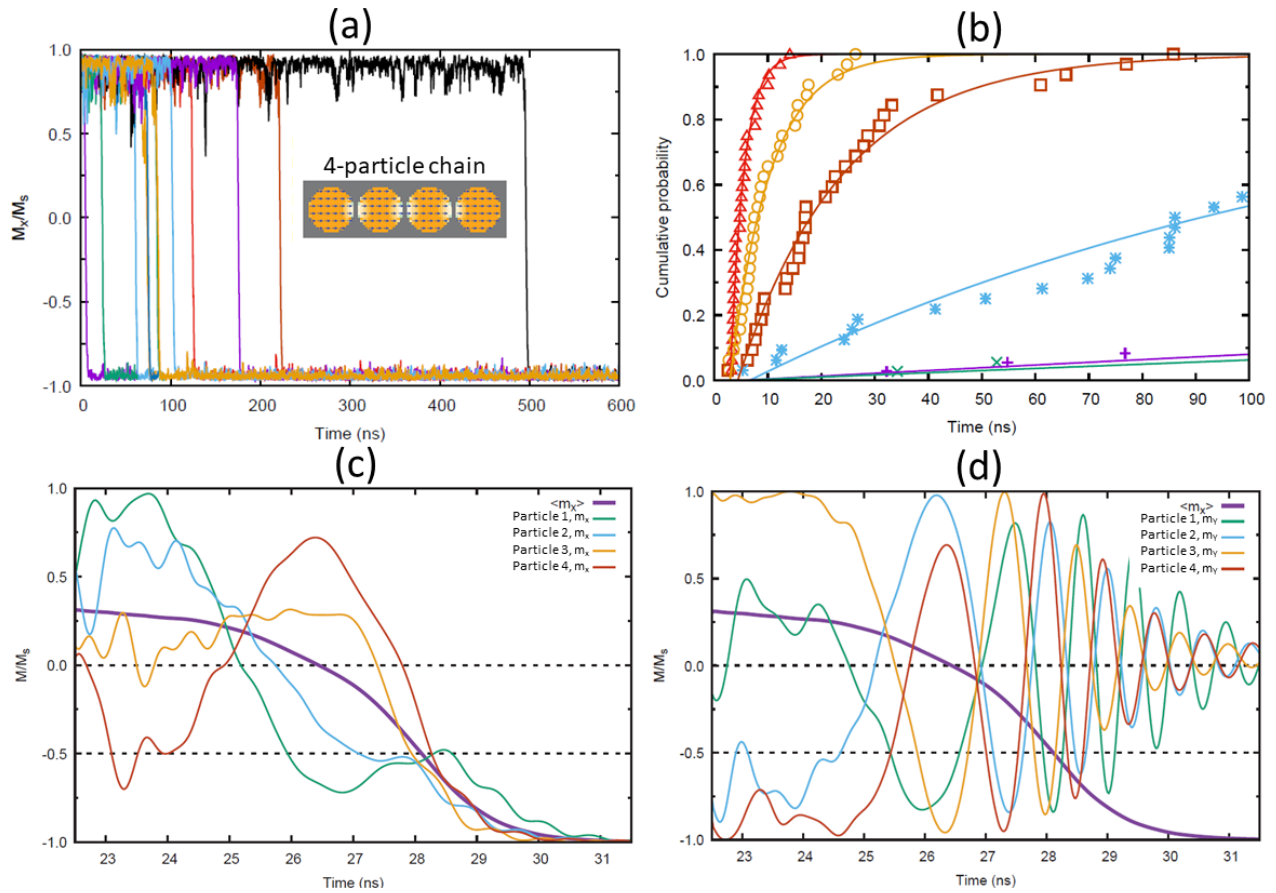


Figure 4. Micromagnetic simulations of thermally activated Néel reversals for chains of four nanoparticles at temperature $T = 290$ K. Individual nanoparticles in the chain are 18 nm diameter spheres, with 2 nm spacing. Discretization cell size is 2 nm. Material parameters $M_s = 480$ kA/m, $A = 13.2$ pJ/m, cubic anisotropy with $K = -13.7$ kJ/m³ and damping coefficient $\alpha = 0.1$, except as noted. (a) 12 trials with reversing field $\mu_0H = 18$ mT. Applied field and chain axis parallel to x -axis. (b) Switching event times accumulated for 32 trials at five different applied fields: $\mu_0H = 30$ mT (red triangles), 26 mT (gold circles), 22 mT (brown squares), 18 mT (blue asterisks), and 14 mT (green crosses and purple pluses). The curve trace marked by (+) has anisotropy $K = 0$ J/m³. Anisotropy for all others is cubic with $K = -13.7$ kJ/m³. (c,d) Detail of switching event with reversal field $\mu_0H = 14$ mT. At $t = 22.5$ ns the chain magnetization has just crossed over the energy barrier, and these curves show the tail of the reversal with the thermal field deactivated (i.e., $T = 0$ K). (c), (d) show the x - (resp. y -) magnetization component for each particle individually (thin curves), along with the x -axis magnetization for the chain as a whole (thick purple curve).

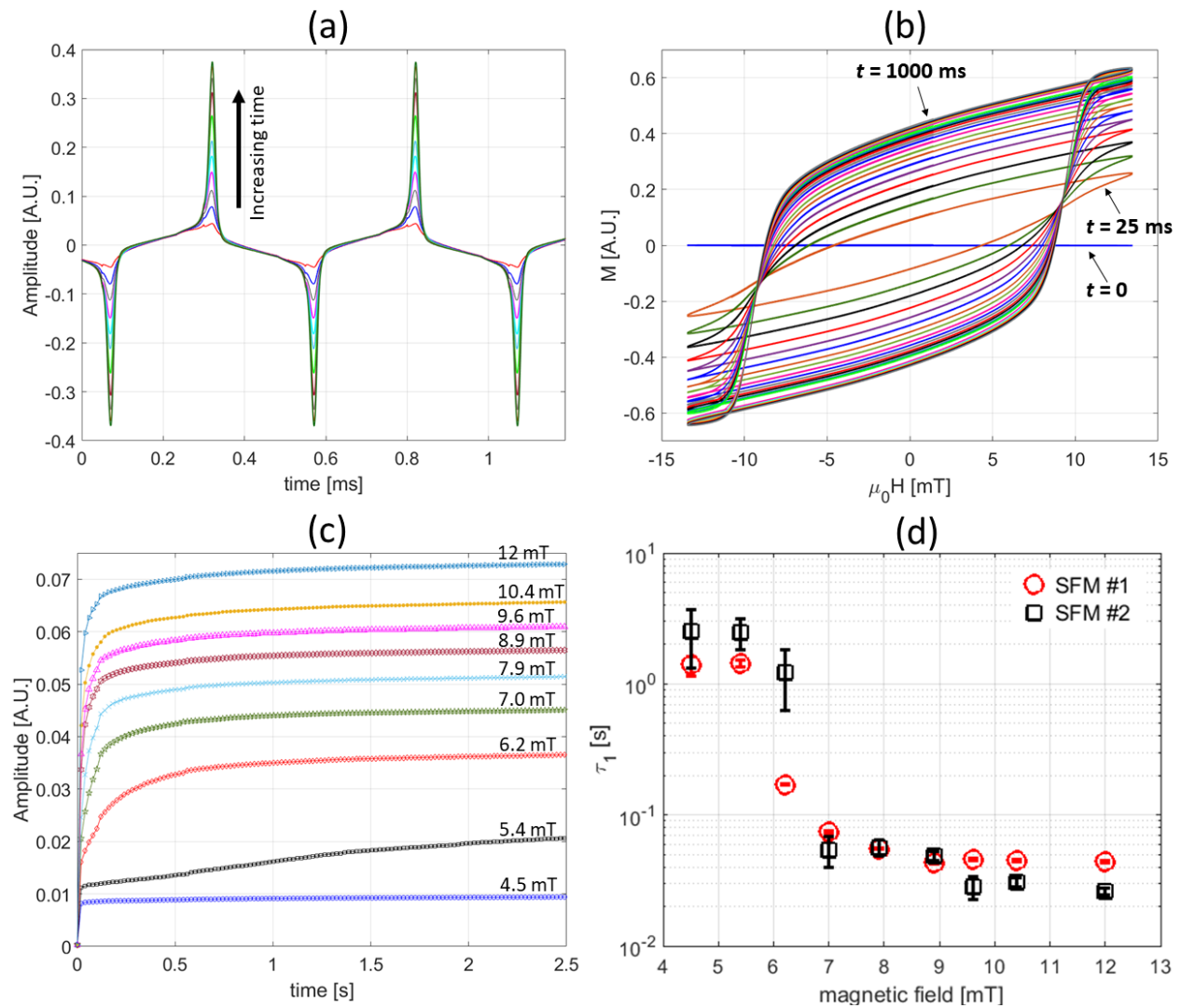


Figure 5. Alignment of chain axis with field axis. (a) dM/dt of SFM sample at 25 ms bin steps at a fixed magnetic field (10 mT, 20 kHz). As time elapses, the amplitude increases until a plateau is reached. (b) Time dependent hysteresis loops for data in (a). (c) Root-mean-square (RMS) of the magnetization response for different magnetic fields and fixed frequency (20 kHz). In proximity of the threshold field (between 4.5 and 6.2 mT), the time dependence displays multi-step behavior, similar to the MRX data. (d) Fits of the fast time constant for data in (c) for both SFM samples show the characteristic threshold behavior. The fitted slower time constant from (not shown) does not change appreciably and varies between 300 ms to 1 s.

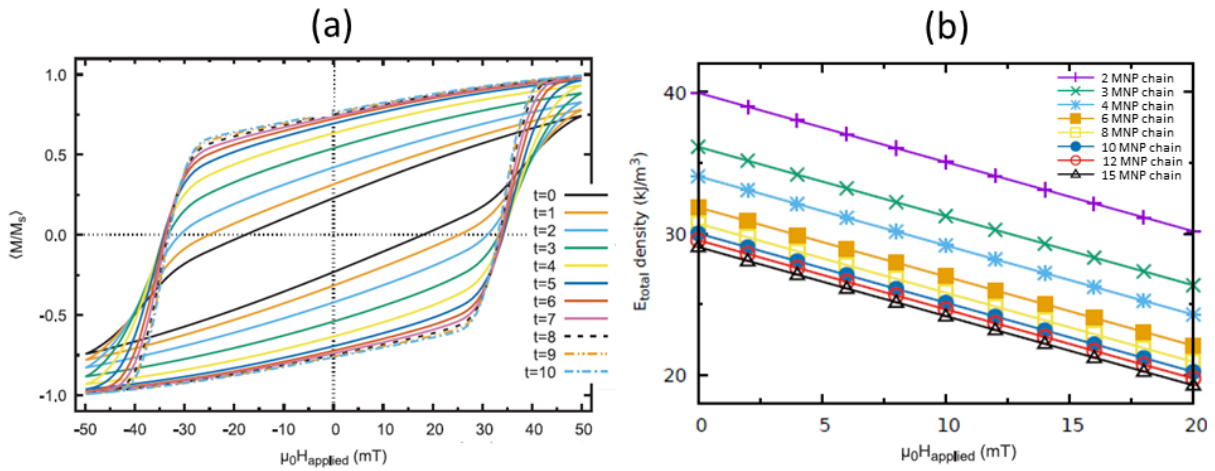


Figure 6. Micromagnetic simulations: (a) Chain rotation: Evolution of hysteresis loops for a population of four particle chains, having random orientations at $t=0$ and gradually rotating by $t=10$ into alignment with the applied field axis (arbitrary time units). Simulations capture the characteristics exhibited in the experimental data in Fig. 5(b). (b) Magnetic energy density as a function of an on-axis applied field for chains with various number of 18 nm nanoparticles, with fixed 2 nm spacing between the nanoparticles.

Methods

Magnetic nanoparticle synthesis and physical characterization

Two methods were used for synthesis of colloidal nanoparticles: Protocol A was used for synthesis of the three samples with diameters 7 nm, 10 nm, 15 nm (SFM #1) and Protocol B was used for synthesis of the 20 nm (SFM #2) sample.

Protocol A is a modified procedure of Sun et al. to synthesize iron oxide nanoparticles via thermal decomposition³⁶. Each synthesis was modified slightly to produce nanoparticles with different sizes. Walter Stern 501 carbon microporous boiling chips were used in the synthesis.

The smallest particles (7 nm, Sample A) were synthesized by mixing 1.695 g oleic acid, 1.605 g oleylamine, 0.70634 g iron acetylacetonate and 2.5844 g of 1,2 hexadecanediol with 15 mL of benzyl ether in a 125 mL volume 3-neck flask. The mixture was attached to Schlenk line and degassed three times with nitrogen until a pressure of 25 mTorr was achieved. For the reaction, the solution was raised to a temperature of 200° C for 2 hours. Then, the solution was heated at a reflux temperature of 298° C for 1.5 hours. During the reaction, the solution was stirred continuously using a magnetic stir bar at 1,150 RPM. After the reaction, the solution was cooled to room temperature and washed 2x with a 1:1 mixture of isopropyl alcohol and acetone.

Sample B (10 nm) was synthesized by mixing by mixing 0.95 g oleic acid, 0.9 g oleylamine and 0.95 g iron acetylacetonate with 10 mL of benzyl ether in a 125 mL volume 3-neck flask. For this reaction, a magnetic stir bar was not used for mixing during the reaction since larger nanoparticles are attracted to the stir bar. Instead, 0.6 mL of boiling chips were added to the reaction vessel. The mixture was attached to Schlenk line and degassed three times with nitrogen until a pressure of 25 mTorr was achieved. For the reaction, the solution was raised rapidly a reflux temperature of 298° C for 1 hours. After the reaction, the solution was cooled to room temperature and washed 2x with a 1:1 mixture of isopropyl alcohol and acetone.

Sample C (15 nm, SFM #1) was synthesized using the same procedure as Sample B, except with an increased mass of each precursor. For this reaction, the precursor masses were 1.21 g oleic acid, 1.14 g oleylamine and 1.2 g iron acetylacetonate. All other conditions were kept the same.

TEM Preparation and Imaging: To prepare samples for TEM, the stock nanoparticle solution was diluted by a factor of 1/50 to 1/100 in toluene. Then, $\approx 20 \mu\text{L}$ of the dilute solution was pipetted on top of a Formvar/carbon coated copper TEM grids (Ted Pella). Imaging was performed using a Tecnai T12 Spirit BT transmission electron microscope with a LaB6 filament.

Protocol B (SFM #2) was developed to produce magnetic nanoparticles with similar SFM properties. Synthesis and characterization details are published in recent work³¹. Briefly this method is similarly based on the thermal decomposition of iron acetylacetonate, using 10 mmol of 1,2 hexadecanediol to produce high crystal quality of particles^{37,38}, in a mixture of 1-octadecene (primary solvent) and oleic acid (surface functionalizing ligand). The sized was tuned by changing the heating rate to produce particles in the desirable interacting/SFM size regime.

AC Magnetometry and Magnetic particle imaging (MPI)

Details of the high speed AC (oscillating and pulsed) magnetometry instrumentation are reported previously²³. Briefly, a custom arbitrary-wave magnetic particle spectrometer was used for characterizing MNPs (magnetic particle spectroscopy and hysteresis) over broad frequency (100 Hz to 50 kHz) and amplitude ($< 50 \text{ mT}$) using both sinusoidal and pulsed fields. The excitation solenoid coil and detection inductive coil are made from low inductance Litz wire. The inductive coil sensor is in a gradiometer configuration. For pulsed field measurements, electronics set a lower limit for a measurable time constant at $\approx 1 \mu\text{s}$.

A custom magnetic nanoparticle imaging (MPI) instrument³⁹ was used to image the phantom for SFM and SPM colloidal solutions displayed in Fig. S3. The excitation AC magnetic field ($f_{excitation} = 31.75 \text{ kHz}$, 10 mT_p) and a spatial selection, gradient magnetic field ($H_{gradient} = 20 \text{ T/m}$ in the x-axis, and 10 T/m in the y-axis and z-axis) were used for the imaging. The gradient magnetic field was generated from a pair of N52 grade NdFeB permanent magnets.

Cryo-TEM

Particles suspended in toluene at room temperature were applied to grids, followed by application of the magnetic field, blotting off excess solution, and vitrification by plunge-freezing. Sample concentrations were diluted by 10 to 100 fold from the native concentration to avoid completely attenuating the electron beam. The SFM behavior is preserved at these dilute concentrations (Fig. S5(d)). Grids were ultrathin continuous carbon on lacey carbon supports (Ted Pella #01824G). Freezing was performed using a manual plunger⁴⁰ with the grid plunged directly into liquid nitrogen to induce flash-freezing (Fig. S6). The liquid nitrogen Dewar was filled to near the top, and the solenoid was suspended roughly 1 cm above the liquid nitrogen surface. A grid was clamped in tweezers and suspended at the midpoint of the solenoid using the plunging apparatus, then $3 \mu\text{l}$ of particle solution was applied to the grid using a pipette. The magnetic field (250 Hz, 15 mT) was then applied, the grid blotted manually for 5 seconds using a thin strip of filter paper while still inserted in the solenoid, and the grid plunged into liquid nitrogen immediately.

Electron microscopy was performed using a Glacios CryoTEM instrument (Thermo Fisher Scientific) operated at 200 kV and a nominal magnification of 36,000 \times . Imaging was performed with a Ceta detector yielding a calibrated pixel size of 0.412 nm. SerialEM⁴¹ was used for automated data collection. Exposures were collected at an electron dose rate of 2360 $nm^{-2}s^{-1}$, using 5 frames of 0.5 seconds each for a total exposure of 2.5 seconds and total electron dose of 5890 nm^{-2} . Motion-correction was performed using the native implementation within Relion⁴².

Micromagnetics simulation (OOMMF)

The micromagnetic simulations were performed using the OOMMF micromagnetic package from NIST²⁵. Except as otherwise noted, the nanoparticles were modeled as 18 nm diameter spherical particles with saturation magnetization $M_s = 480 \text{ kA/m}$, exchange constant $A = 13.2 \text{ pJ/m}$, magnetocrystalline anisotropy constant $K = 0 \text{ J/m}^3$, and Gilbert damping parameter $\alpha = 0.1$. Discretization cell size was set at 1 nm, well below the exchange length $l_{ex} = \sqrt{2A/(\mu_0 M_s^2)} = 9.5 \text{ nm}$ typically recommended as the upper limit for discretization. Quasi-static computations for hysteresis loop simulations were performed via conjugate-gradient energy minimization, and thermal studies used a 2nd order Heun method to integrate the stochastic Landau-Lifshitz-Gilbert equation with thermal field of the Langevin type.²⁴ The particle orientations are held fixed in all the micromagnetic simulations, so magnetization reversals are necessarily of the Néel type.

Chain rotation simulation: To model the rotation of a collection of nanoparticle chains, hysteresis loops for individual 4-bead chains at various angles to an applied field are computed. Geometric and compositional differences between chains are allowed by averaging each loop against copies of itself scaled to have coercive fields normally distributed with relative variance 0.01. The response of a collection of chains with varying orientations can then be computed by summing hysteresis loops corresponding to the individual orientations. The evolution of an ensemble of chains are modeled by gradually rotating each chain in proportion to the torque on it from the applied field. The magnetic response from a background population of isolated superparamagnetic particles are included to provide a non-hysteretic upward cant (slope) to the response.

Magnetostatic energy of chains: The energy decrease afforded by nanoparticle chaining is caused primarily by a local reduction in the magnetostatic energy near neighboring nanoparticles, as shown in Fig. S10(c). The 32 kJ/m^3 energy density volumes in the center of the nanoparticles (orange) is mostly self-magnetostatic (i.e. shape anisotropy) energy from the individual particle. The lower energy regions (-32 kJ/m^3 , green) represent inter-particle stray field interactions. This latter effect quickly dissipates with increased spacing between the particles (upper vs. lower figure)

Supplementary information, SI

MPI imaging spatial resolution

The imaging spatial resolution is a function of the gradient field, $G(x,y,z)$, and the point-spread-function, PSF^{43,44}. The resolution advantage of SFM over SPM nanoparticles is presented in Fig. S3. The MPI images are acquired using a glass phantom (Fig. S3(a)) containing 10 μL colloidal MNP solution. 2D-slice images of the 3D glass phantom for the SPM and SFM systems are presented in Figs. S3(b) and S3(c), respectively. These MPI images shows the superior spatial resolution of the SFM system relative to the SPM system. Figure S2(a) shows the order-of-magnitude magnetization enhancement of SFM relative to SPM.

The point-spread-function (PSF), which correlates with the imaging spatial resolution, is measured in Fig. S8(a) and S8(b) for the SPM and SFM systems, respectively. Relative to SPM particles, SFM particles exhibit exceedingly narrow PSFs at and above the threshold field up to $\approx 10x$ narrower than the SPM case. Furthermore, SFM systems display greater dependencies on magnetic field amplitude. The magnetic field amplitude has a larger impact on the PSF width in the SFM case than in the SPM case. Figure S8(c) show the fitted PSF full-width-half-maximum (FWHM) comparison for SFM and SPM samples. The most notable feature is the sharp drop in the FWHM for the SFM sample at the threshold field, which marks the onset of SFM behavior. Figure S8(d) is the ratio of the two curves in S8(c), which shows the resolution enhancement factor. This trend displays a strikingly similar behavior to that reported in¹⁴, indicating a common origin in the particle response at variable field amplitude, despite being two independently synthesized colloidal systems using different synthesis protocols.

Micromagnetics simulations of switching times

If the switching events follow a Néel-Arrhenius relation,

$$\tau_N = \tau_0 \exp\left(\frac{E_B}{k_B T}\right) \quad (4)$$

where τ_N is the mean switching time, τ_0 is the attempt period, E_B is the height of the energy barrier, k_B is the Boltzmann constant, and T is the absolute temperature, then the cumulative distribution function (CDF) has the form

$$\text{CDF}(t) = 1 - a^{(t-b)} \quad (5)$$

where b is a spin-up time (an offset to allow for thermal motion away from the initial magnetization configuration) and $a = 1 - 1/\tau_N$. Thus, fitting Eq. 5 to curves in Fig. 4(b) allows the extraction of τ_N as

$$\tau_N = (1 - a)^{-1}. \quad (6)$$

The shape anisotropy of the chain produces an energy barrier to magnetization reversal; Figures. S9(a) and S9(b) studies the effect of this barrier on reversal. The green trace in Fig. S9(a) tracks the overall chain magnetization across the reversal event. The thicker purple trace, H_{switch} , reports at each time index the strength of the field that would be necessary to complete the reversal from that magnetization configuration if the thermal field were removed. For example, in the initial configuration at $t = 0$ ns, a field of approximately 32 mT would be required. (Which is also the $T = 0$ K coercive field.) Not much changes for the first 20 ns, but between 20-25 ns H_{switch} drops, indicating that the magnetization configuration is effectively climbing up the energy landscape. At $t = 11.5$ ns the configuration clears the $\mu_0 H_{\text{app}} = 14$ mT energy barrier. Beyond this point the reversal can proceed without the thermal field (Figs. 4(c) and 4(d)). Note that the shape of the energy landscape depends on the strength of the reversal field. To complete the reversal without either the applied or thermal fields requires waiting until $t = 26$ ns, where $M_x/M_s = 0$.

Figure S9(b) examines directly the energy terms in the simulation. The energy from the applied field (E_{Zeeman}) and self-magnetostatic (E_{demag}) terms are considered; the magnetization in each particle is nearly uniform, so the exchange energy contribution is quite small. The shape anisotropy arises from the self-magnetostatic energy term (blue trace), and represents the barrier to reversal with no applied field. In this example that barrier is 120 zJ, or $30 k_B T$ at 290 K. Applying a 14 mT reversing field reduces the barrier to approximately $12 k_B T$. This value can be combined with a τ_N estimate from Table S9(c) and Eq. 4 to approximate τ_0 .

SI Figures and Figure Captions

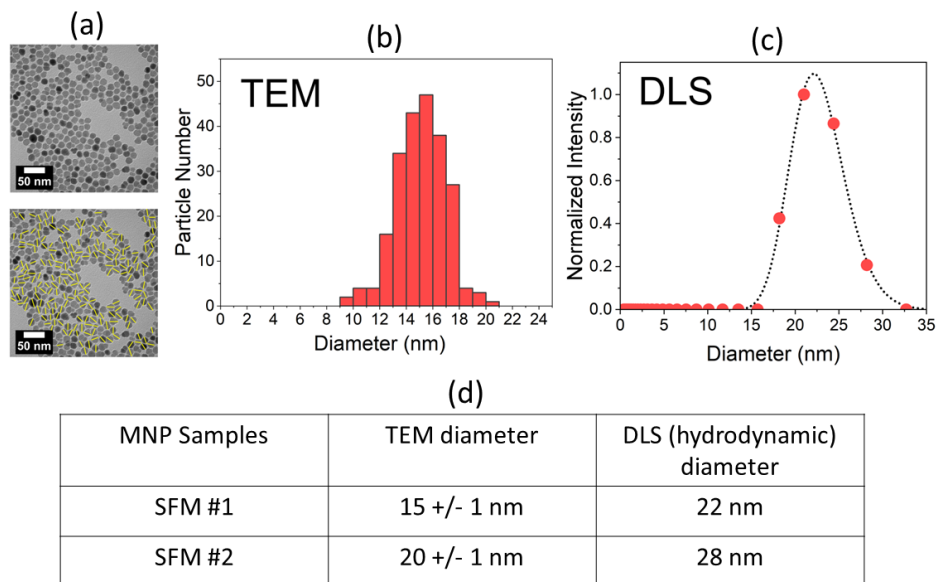


Fig. S1. Physical characterization of two SFM nanoparticle systems. (a) TEM images of SFM #1 (top) and selected particles for determining size distribution (bottom). (b) TEM diameter distribution of 100 nanoparticles for the SFM #1 sample. (c) DLS diameter distribution of nanoparticle solution for the SFM #1 sample. (d) Table summarizing the size distribution of two SFM samples in this work. The values for SFM #2 in (d) and additional physical characterization information can be found in reference³¹. The DLS measurements do not include a standard deviation due to the presence of multiple aggregated populations.

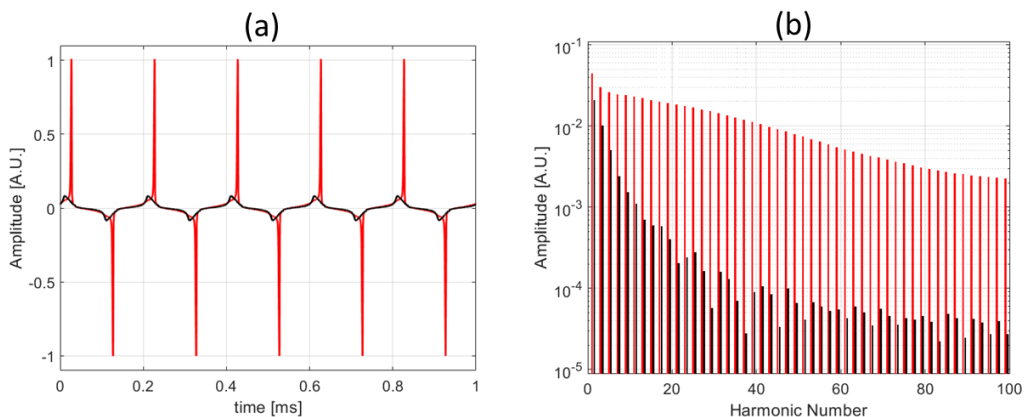


Fig. S2. AC magnetometry of SFM (red) vs SPM (black) systems using a sinusoidal field at 10 kHz and 10 mT. (a) $V_i(t)$ of the SFM system displays sharp narrow peaks relative to SPM and a phase offset. (b) Fourier transform of (a) shows a significantly broader harmonic spectrum for the SFM system (red) compared to the SPM system (Vivotrax, black).

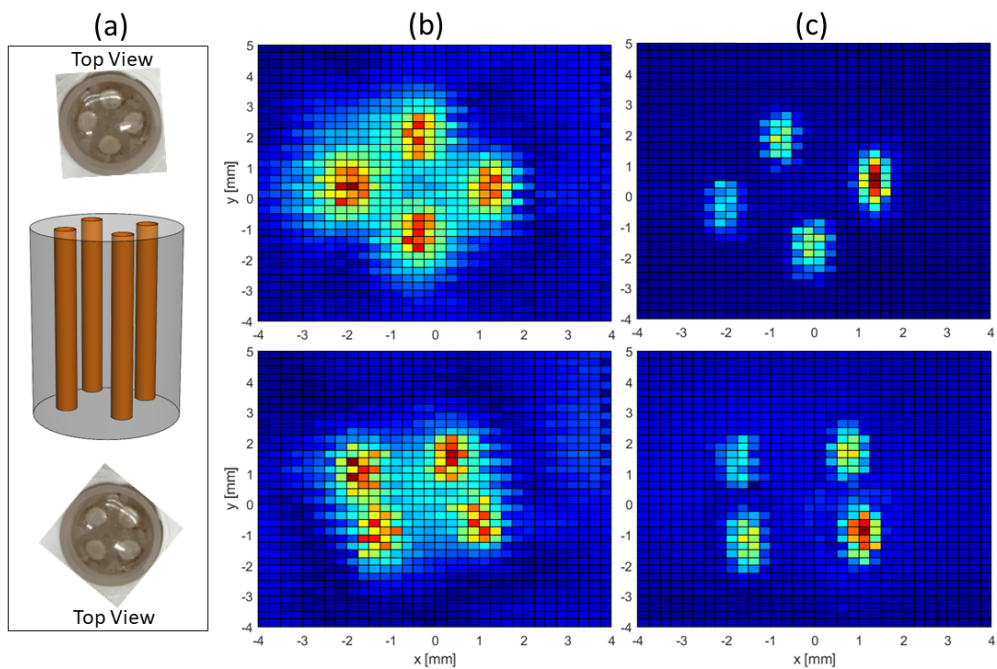


Fig. S3. Magnetic particle imaging (MPI) for colloidal MNP solution using (a) a glass phantom of (b) a commercial SPM system (Vivotrax) and (c) synthesized SFM #1 system. Undiluted colloidal MNP samples fill the four wells in the glass phantom (gold color). In the 2D-slice MPI image of the phantom, the four wells are blurred for the SPM but clearly resolvable in the SFM system. The upper and lower rows of the MPI image in (b) and (c) correspond to rotated configurations of the phantom indicated by the top views of the phantoms in (a).

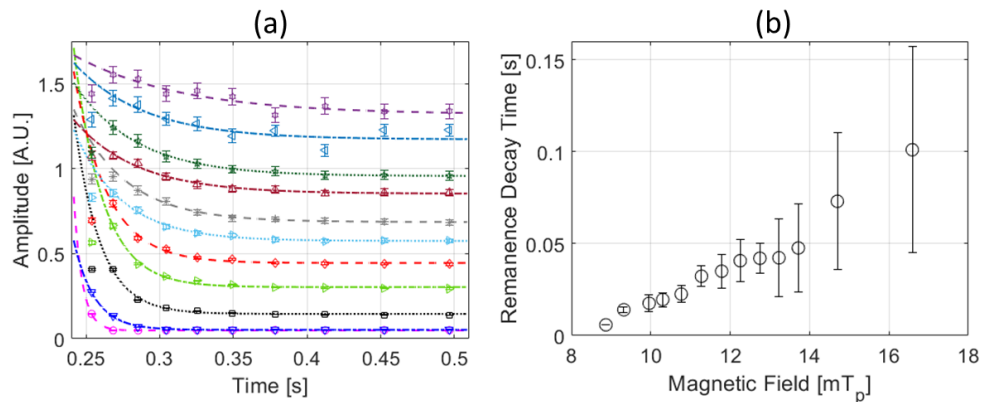


Fig. S4. (a) Remanence decay curves for SFM particles at different magnetic fields. (b) Fitted decay time constants as a function of magnetic field. The fitting function is a single exponential with an offset. The increased remanence lifetime with increasing amplitude indicates a memory effect.

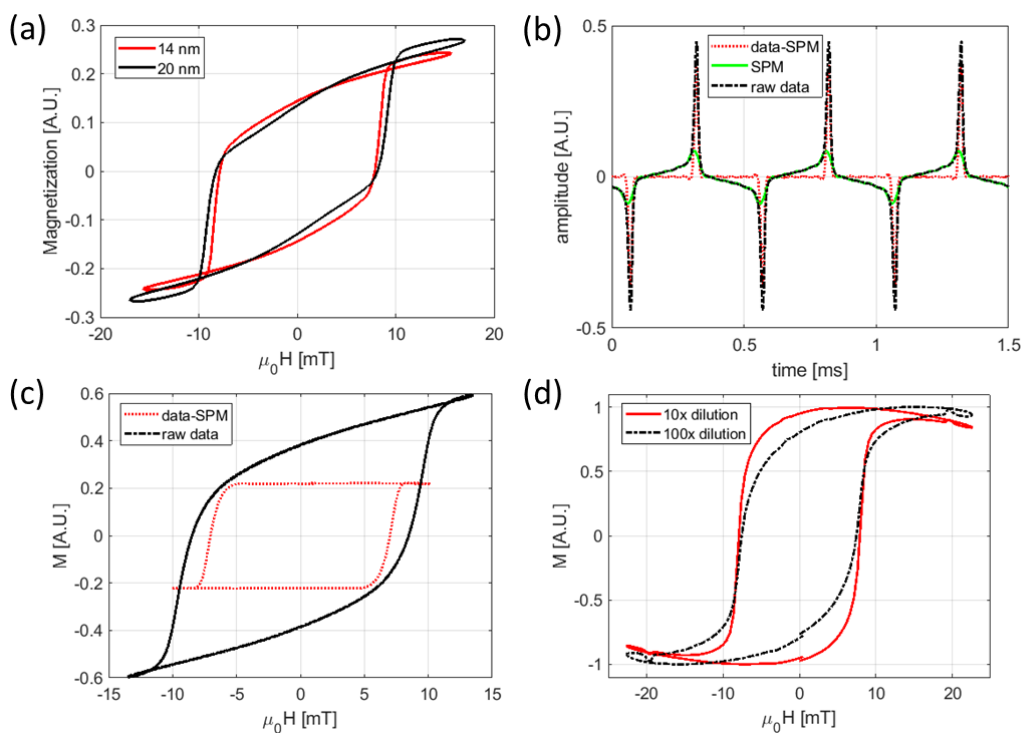


Fig. S5. (a) Hysteresis loops of two independently synthesized SFM samples (15 nm and 20 nm) at a 5 kHz magnetic field. The hysteresis loops are canted square loops displaying both SPM (slope) and SFM-like behavior (square). (b) Contribution of magnetization responses from both isolated (SPM) particle and chained (SFM-like) populations. Raw data of the time response of 15 nm sample (black, dash-dot line) with SPM contribution (green, solid) subtracted, leaving behind only the chained particle response (red, dot line). (c) hysteresis loop of the raw data for the 15 nm sample (black, dash-dot line) with SPM response subtracted (red, dot line). The positive linear slope in the raw data is from the single particle (SPM) response. (d) Square-like hysteresis loops suggests that SFM behavior is preserved at a 100-fold dilution for the cryo-EM experiment.

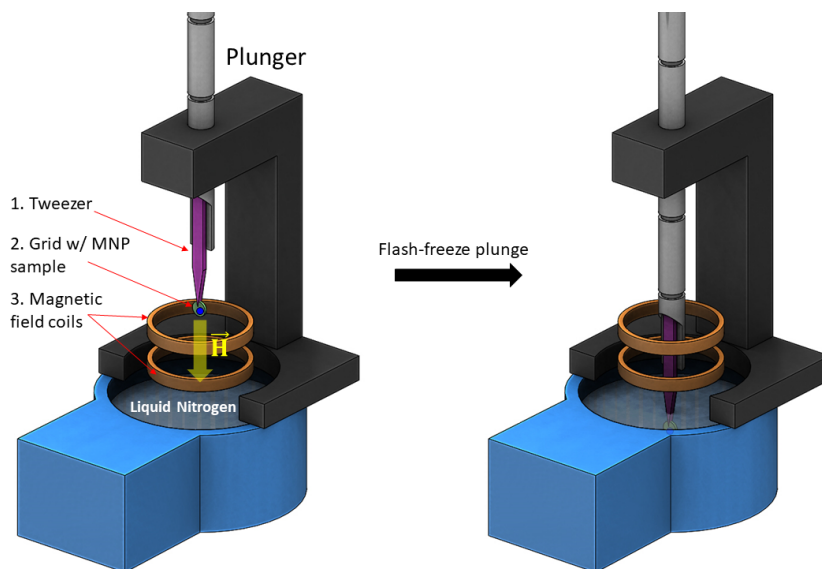


Fig. S6. CryoEM flash-freeze plunger method. A manual plunger equipped with a tweezer holds the sample grid (green disc) and a drop of MNP sample (blue circle). The AC magnetic field (250 Hz, 15 mT) is turned on about 5 seconds prior to plunging the sample grid into the liquid nitrogen bath for cryo-freezing.

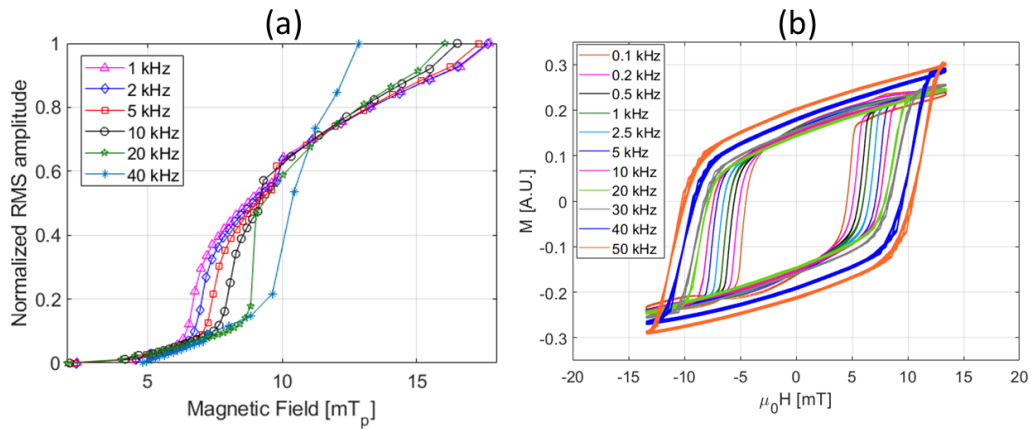


Fig. S7. Frequency dependence of (a) threshold and (b) hysteresis loop for SFM particles for a fixed amplitude of 10 mT. The threshold field shifts higher with increasing frequency because it takes more energy to undergo physical rotation by Brownian motion at an increased rate towards chaining. In (b), SFM behavior persists down to frequencies 100 Hz.

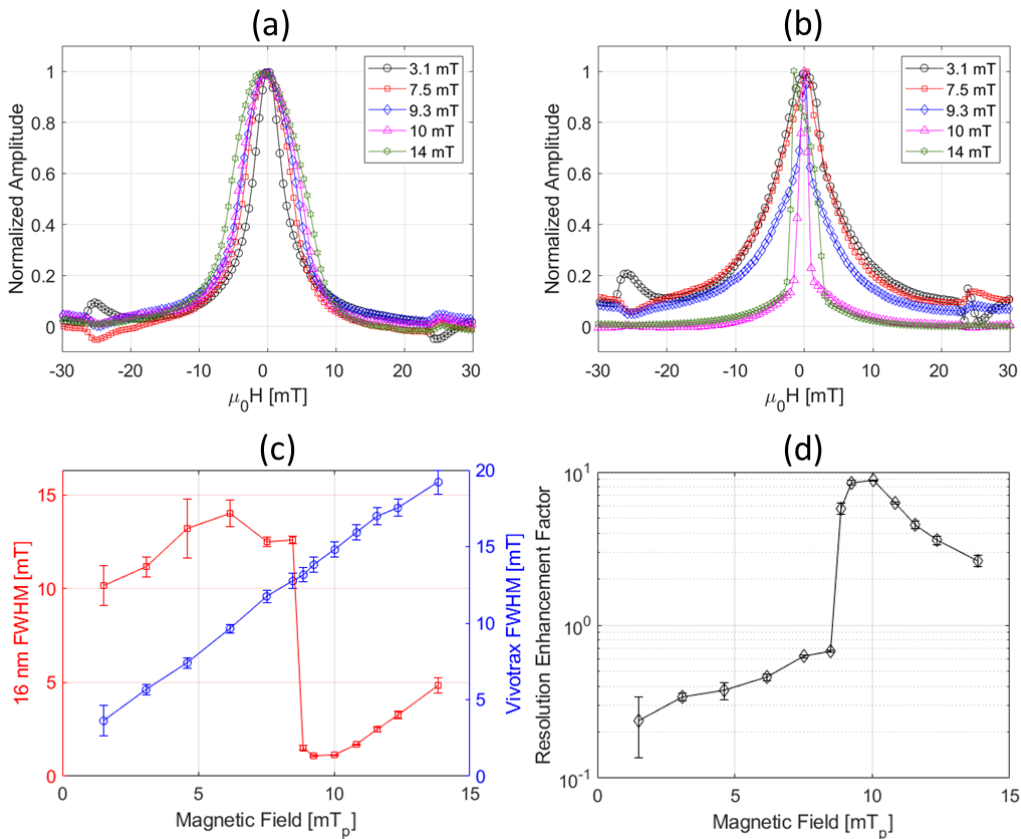


Fig. S8. Amplitude dependence of PSF for Vivotrax (a) and SFM #1 (b) measured at 20 kHz. For the SFM system, an abrupt change in the PSF at and above the threshold field is indicative of chaining. (c) The field dependence of the PSF's fitted FWHM for SFM #1 and SPM (Vivotrax) systems. (d) The resolution enhancement factor by taking the ratio of the two curves in (c).

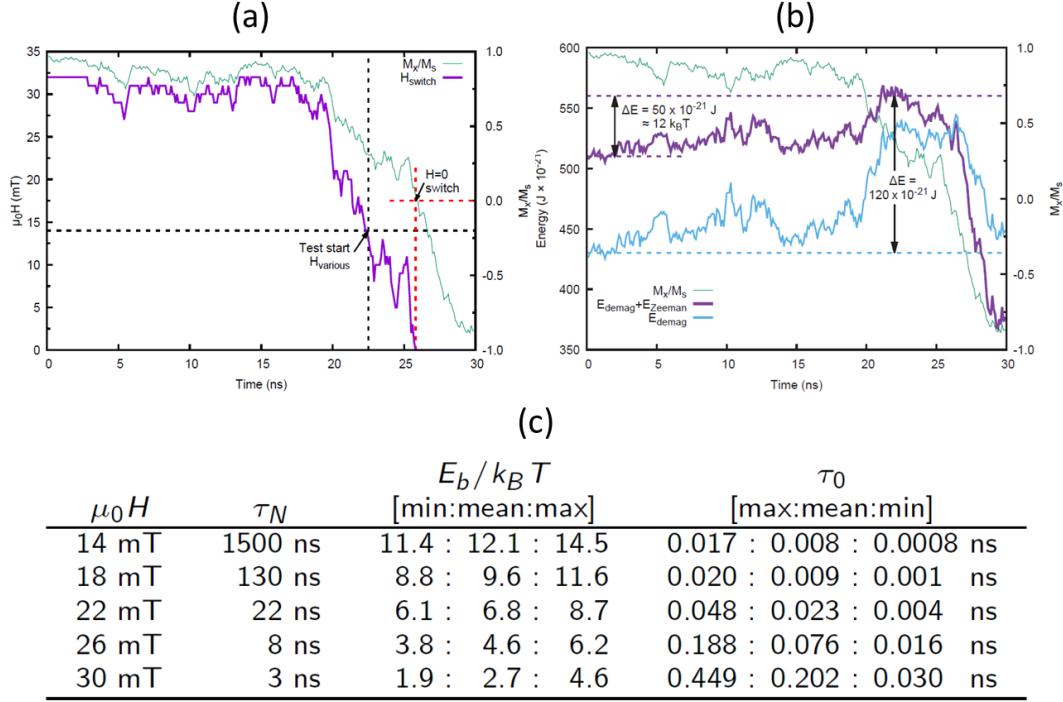


Fig. S9. (a) Thermal reversal event used as base for subfigures 4(c) and 4(d) in the main text. The green trace corresponds to the solid purple trace in 4(c) and 4(d), but with the $T = 290 \text{ K}$ thermal field engaged throughout. The purple trace maps the minimal applied field needed to reverse the chain from that time index if the thermal field were deactivated. The point marked "Test start" is the starting point for subfigures 4(c) and 4(d). (b) The self-magnetostatic and applied field energy components for the reversal event depicted in subfigure (a). (c) Table of fitted constants for the 5 simulated trials from 4(b). For each magnetic field, τ_N and the barrier height E_b are fitted. The attempt time, τ_0 , is calculated using Eq. 4. Estimated uncertainties are provided for energy barrier and attempt time constants.

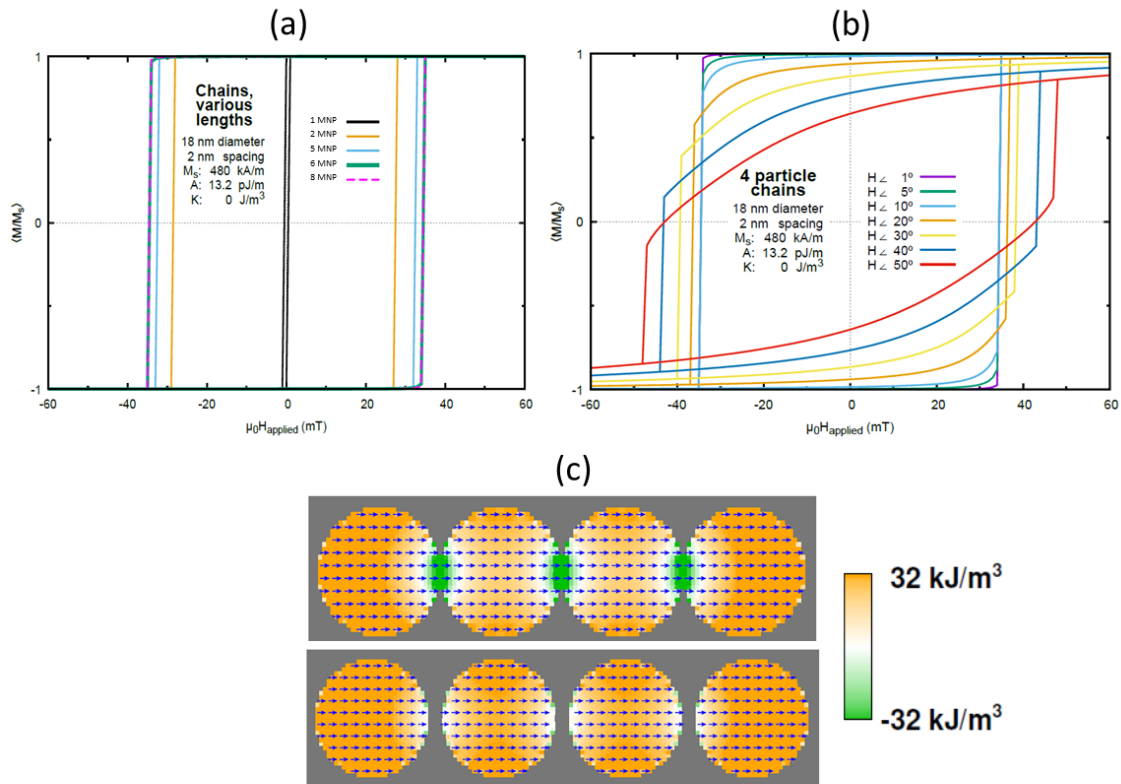


Fig. S10. Micromagnetic simulations comparing chain growth vs chain rotation mechanisms. (a) Evolution of hysteresis loop with increasing chain length. The coercivity increases rapidly from monomer to dimer, but saturates with increasing particle number. (b) Evolution of hysteresis loops as a function of angle of the chain axis relative to the field axis. The increase in coercivity and remanence is gradual with angle rather than abrupt and is more consistent with data in Fig. 5(b). Here, the simulation is for single chains at different angles, rather than the ensemble average of chain populations in Fig. ??(a); ensemble averaging leads to a smoother hysteresis curve. (c) Spatial variation in energy density for two 4 nanoparticle chains with no applied field. The nanoparticles are 30 nm across, with 0 nm and 4 nm spacing in the upper and lower figure, respectively.